Journal of Materials Chemistry A

ROYAL SOCIETY OF CHEMISTRY

PAPER

View Article Online
View Journal | View Issue

Check for updates

Cite this: J. Mater. Chem. A, 2025, 13, 8549

Multifunctional broadband emitters based on rare earth phosphors for all-weather and efficient radiative cooling and energy saving†

Qinglong Hu,[a] Ruiming Tan,[a] Pengjie Zhong,[a] Keyu Han, *[a] Yinyan Li, [b] Peng Xue*[c] and Gongxun Bai *[a]

Received 17th December 2024
Accepted 10th February 2025

DOI: 10.1039/d4ta08945f

rsc.li/materials-a

Passive daytime radiative cooling (PDRC) presents an effective strategy for mitigating the global greenhouse effect. However, some existing PDRC systems necessitate complex designs and are limited to selectively radiate heat into outer space. To improve the performance of PDRC systems, we have developed a multifunctional rare earth phosphor film that integrates particle scattering, fluorescence emission and broadband radiation capabilities. Outdoor tests conducted under an average solar radiation of 644 W m^{-2} indicated that the film achieved a sub-ambient cooling temperature of 8.26 °C with a net cooling power reaching up to 101 W m^{-2}. During night tests, the SM film's average cooling was only 0.29 °C, which is promising for real-life nighttime comfort and building service life. Given its superior performance and multifunctionality, the composite film demonstrates significant potential for application in contemporary green development initiatives.

1 Introduction

As the greenhouse effect keeps intensifying, it presents fundamental economic, health and security risks to human civilization.[1,2] Maintaining a habitable built environment has emerged as one of the most pressing challenges of our era.[3,4] Traditional temperature regulation primarily relies on heating, ventilation and cooling systems.[5–7] Nevertheless, cooling and heating consume a considerable amount of energy and release a substantial quantity of greenhouse gases, which account for over 30% of global energy emissions.[8–12] In light of these issues, development of an environmentally sustainable cooling solution that does not consume energy and does not produce emissions has become a matter of urgency. Passive daytime radiative cooling (PDRC) has garnered significant attention from researchers in recent years owing to its efficient cooling performance.[13] This technology achieves radiative cooling by utilizing its superior reflectivity in the visible range and superior emissivity in the infrared range. Furthermore, PDRC can achieve cooling by radiating energy into outer space through an atmospheric window (8–13 μm).[8,13,14] The temperature of the universe is approximately −270 °C, while the Earth's surface temperature is roughly 27 °C. The substantial temperature disparity between the Earth and outer space enables the planet to lower its temperature by emitting energy through the atmospheric window.[15–18]

Recently, numerous PDRC materials and structures have achieved outstanding accomplishments in their high reflectivity and high emissivity. Some examples include rare earth phosphor materials,[13,18] multilayer photonic structures,[19] porous polymer materials,[20,21] aerogels,[22,23] and particle polymer coatings.[17,24] Typically, polymer materials exhibit outstanding radiative properties in the infrared band, and hence, they are frequently utilized as radiative cooling materials.[25,26] By incorporating nanoparticles into polymers, radiatively cooled films with excellent reflectivity and emissivity can be fabricated.[13,17,26] To enhance the cooling efficacy of devices, many researchers have focused on selective coolers with excellent emissivity within the atmospheric transparency window region. For instance, Wu *et al.* developed a dual-frequency radiative cooling device with enhanced thermal emitting performance, which reduced the temperature by 9 °C.[27] Wang *et al.* created a composite film with a rational pore structure. The composite film exhibited selective radiative cooling during the daytime and realized a cooling effect of 14.9 °C.[28] Thus, these studies reported materials with significant radiative cooling performance. However, their design is based on selective narrow-band radiation, which only focuses on cooling during the day and ignores the problem of excessive cooling at night. Excessive cooling at night not only causes discomfort to the human body,

[a]College of Optical and Electronic Technology, China Jiliang University, Hangzhou 310018, China. E-mail: hanky@cjlu.edu.cn; baigx@cjlu.edu.cn

[b]Key Laboratory of Rare Earth Optoelectronic Materials and Devices of Zhejiang Province, China Jiliang University, Hangzhou 310018, China

[c]Beijing Key Laboratory of Green Building Environment and Energy Saving Technology, Beijing University of Technology, Beijing 100124, China. E-mail: xp@bjut.edu.cn

† Electronic supplementary information (ESI) available. See DOI: https://doi.org/10.1039/d4ta08945f

but also reduces energy efficiency due to the need for additional heating.

To address these issues, we constructed a multifunctional rare earth phosphor PDRC film based on polydimethylsiloxane (PDMS), which possesses excellent mid-infrared emissivity and self-cleaning properties.[29] During the preparation process, TiO_2 nanoparticles were selected for their high spectral reflectance in the solar spectrum.[30] However, TiO_2 particles in the wavelength range of 0.25 to 0.40 μm exhibit significant solar absorption, resulting in a total solar reflectance of less than 0.90 for the entire cooler, and are thus insufficient to mitigate heat from solar radiation for achieving efficient PDRC.[31,32] To address this issue, we incorporated efficient and cost-effective rare earth phosphors (REPs) as a filler that can effectively compete with TiO_2 nanoparticles in absorbing ultraviolet (UV) light and subsequently emitting it as blue light at a wavelength of 470 nm. This approach mitigates the temperature rise associated with solar energy absorption.[31] By employing this method, we overcome the limitations of traditional coating materials in achieving exceptionally high solar reflectivity. Additionally, glass microspheres (GMs) were introduced as an additional filler to create three distinct sizes of fillers alongside TiO_2 nanoparticles and REPs. This strategy promotes multiple scattering due to the large broad size distribution of inorganic particles within the polymer matrix.[17] Hence, the film reflectance reached 0.93, and its average emittance in the mid-infrared range was recorded at 0.94, which is particularly notable at the atmospheric transmittance window where it was measured at 0.95. The outdoor test with an average solar radiation of 644 W m^{-2} shows that the film's sub-ambient cooling temperature is 8.26 °C. Furthermore, the inclusion of broadband radiation allows the SM film to better absorb down to the long wavelength radiation range from the atmosphere at night, providing a heating effect to the building. In the nighttime test, the average temperature difference of the SM film was only 0.29 °C, effectively mitigating the circumstance of nighttime supercooling. In addition, our designed films demonstrated exceptional flexibility, hydrophobicity (static water contact angle: 120°) and self-cleaning properties under a series of tests.

2 Results and discussion

As illustrated in Fig. 1a, the SM film serves as an effective cooling coating for building surfaces by dissipating heat during the daytime, maintaining a comfortable living environment. Meanwhile, excessive cooling can be inhibited during the nighttime, indicating its promising potential for practical applications. In Fig. 1b, we assume an ideal emissivity of 1.0 for a broadband radiator at 3–40 μm and 1.0 for a selective emitter at 8–13 μm. The blackbody radiative spectrum at 32 °C was further calculated, which provides a theoretical foundation for subsequent calculations. In order to better reflect the excellent performance of the SM film, we set the atmospheric downward long-wave power to 400 W m^{-2}.[33–35] Under typical environmental conditions, the heat transfer coefficient h usually falls within the range of 2–10 W m^{-2} K^{-1}. For still air or natural

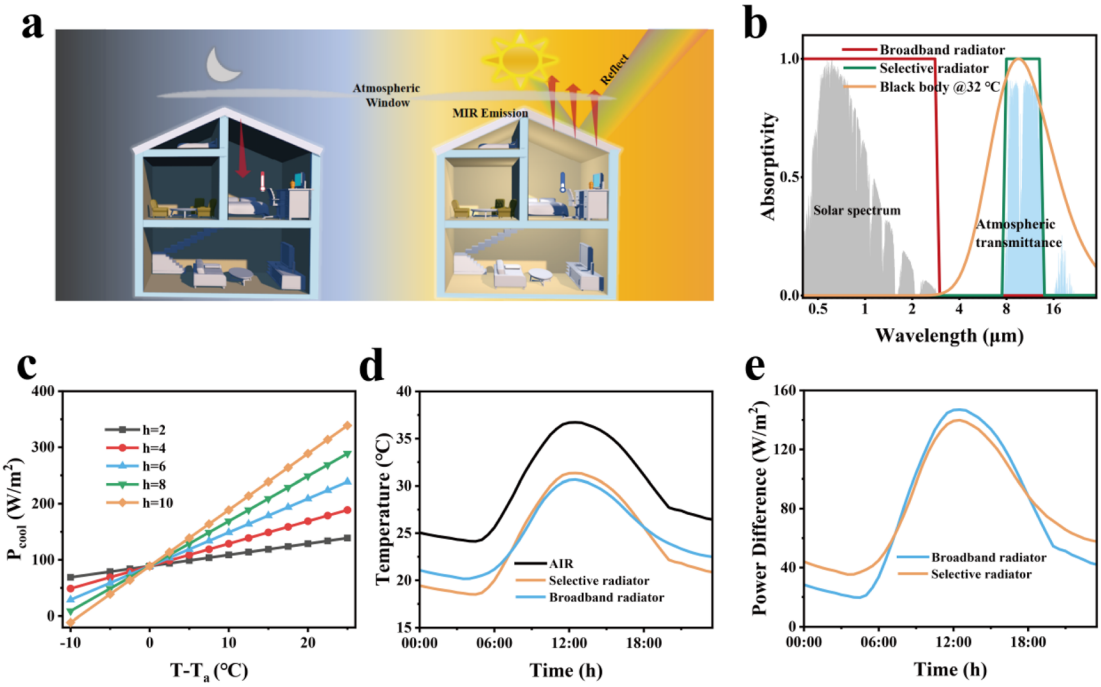

Fig. 1 Application diagram and simulation analysis of the PDRC samples: (a) schematic demonstrating the application scenario of the SM film. (b) Standard solar spectrum, IAM1.5 (λ) (gray), atmospheric transmission spectrum, T_{atm} (λ) (blue), ideal absorption spectrum, DRC (λ) of the broadband radiator (red) and selective radiator (green), and blackbody radiation spectrum at 32 °C, B (λ, 32 °C) (orange). (c) Variation in cooling power with different h values. (d) Cooling temperatures of the selective and broadband radiators calculated and compared with the ambient temperature. (e) Calculation of $P_{rad} - P_{atm}$ for the selective and broadband radiators.

convection conditions, h is typically between 2–5 W m^{-2} K^{-1}, while in conditions with higher wind speeds, h can reach up to 10 W m^{-2} K^{-1}. We chose 4 W m^{-2} K^{-1}, because it reflects the heat convection conditions in common environments and aligns most closely with the experimental data. When the cooling temperature reaches 8.26 °C, the cooling efficiency obtained by COMSOL simulation calculation is 105 W m^{-2}. According to the actual test results, the net cooling efficiency is 101 W m^{-2}. This consistency validates our theoretical calculations and establishes their scientific credibility. Our detailed calculation results (Fig. 1c) show that the cooling power increases with the temperature difference and h_c values. Fig. 1d and e are calculated based on the results from Fig. 1b. Fig. 1d shows the cooling effect of two radiation coolers in one day. The temperatures of the broadband radiator and the selective radiator dropped by 18 °C and 16 °C at 2:00 PM, respectively. Notably, the broadband radiator outperforms its selective counterpart in terms of cooling efficiency. The $P_{rad} - P_{atm}$ power outputs from both types of radiators (Fig. 1e) under the h value of 4 W m^{-2} K^{-1} further demonstrate that the performance metrics favoring the broadband radiators over the selective ones persist. Fig. 1e provides a better quantification of the performance of the two PDRC coolers on their effects of heat exchange with the sky (*i.e.* $P_{rad} - P_{atm}$).[36,37]

As illustrated in Fig. 2a, SEM was employed to examine the microscopic cross-section of the SM film, with the GMs and REPs highlighted in green and red with false colors, respectively. Fig. 2a demonstrates that the REPs, GMs and TiO_2 are uniformly distributed throughout the composite film. Fig. 2b shows the SEM images of TiO_2, GMs and REPs, revealing the microscopic morphology and particle size of these three particles. As shown in Fig. S2,† we also examined the EDS spectra of these particles to analyze their elemental composition. By comparing their element content, we can more intuitively assess whether the materials meet the requirements of our experiment. Fig. 2c and d present the simulated data graphs of the particle scattering efficiency of TiO_2 and GMs generated using MATLAB. It can be seen from the data diagram that the scattering efficiency of TiO_2 particles shift to the right as the particle size gradually increases, accompanied by a decreasing

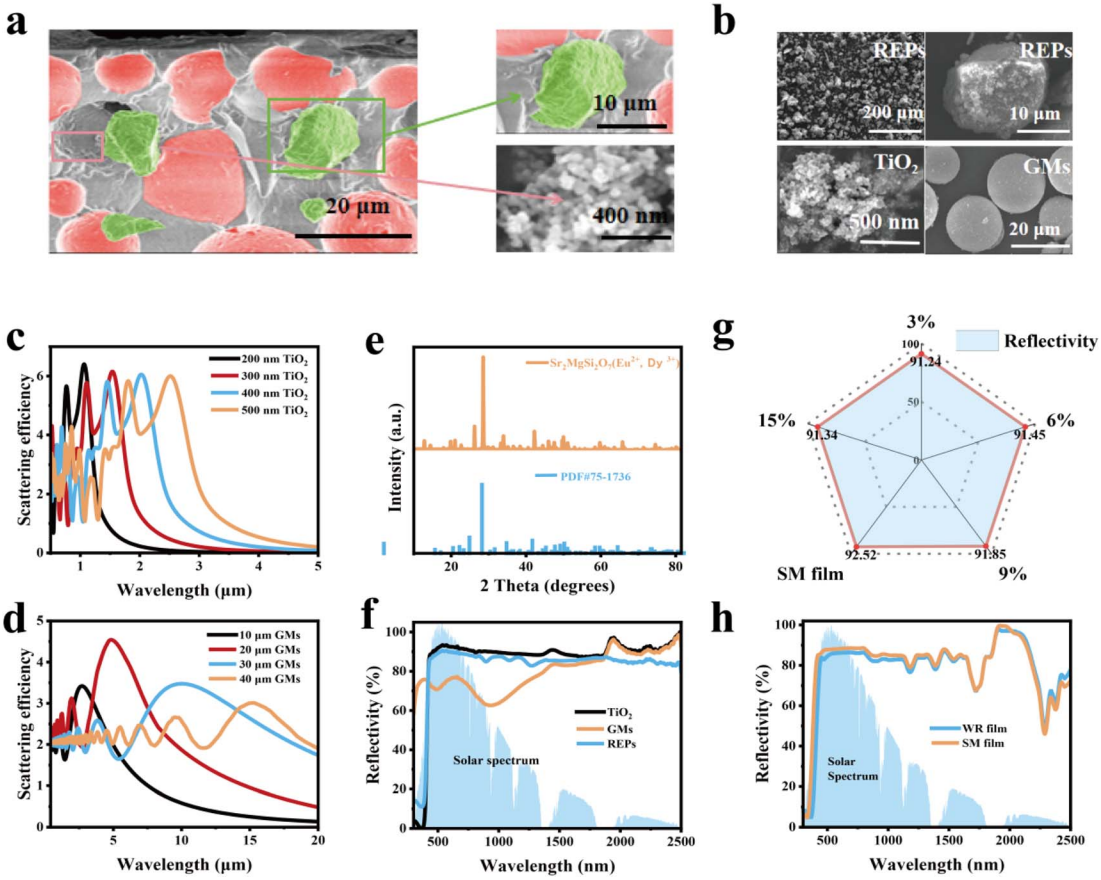

Fig. 2 Micro-morphological images and optical properties of the sample films: (a) false color SEM image of the SM film. The image on the left shows the cross-sectional features of the SM film, and the image on the right shows the locally enlarged image corresponding to the left frame. The green particles represent REPs and the red particles represent GMs. The view at the lower right corner is the microscopic morphology of TiO_2 in the SM film. (b) SEM images of the REPs particles, TiO_2 particles and GMs particles. The upper image on the right is the enlarged image of REPs. (c) Simulated scattering efficiency of the TiO_2 particles. (d) Simulated scattering efficiency of the GMs particles. (e) XRD spectral data plot of the REPs powder. (f) Reflectance test of the GMs particles, TiO_2 particles and REPs particles under the superposition of standard solar spectra. (g) Plot of the average reflectance data of SM films prepared with different REP contents. (h) Reflectance spectra of the SM film and WR film.

trend. Furthermore, when comparing the refractive indices of several commonly used particles (Fig. S3†), the TiO_2 particle refractive index is the best and most in line with our experimental requirements. Therefore, the TiO_2 particles with sizes of 200 nm or 300 nm meet our requirements. In the particle size analysis test, we determined that the particle size of the GMs is 10–30 μm. According to high-order Mie resonance excitation,[30,38] GMs of varying sizes embedded in PDMS films can collectively enhance the scattering efficiency of the cooler. The particle size analyses conducted on both TiO_2 and GMs indicate that their dimensions align with the simulation results (Fig. S4†).

The XRD pattern of REPs, with characteristic peaks perfectly matching those of the standard card (Fig. 2e), demonstrates that the REPs powder has excellent purity and effective optical properties. As shown in Fig. 2f, reflectance tests were conducted on TiO_2, GMs and REPs; all of which exhibited outstanding performance characteristics. Notably, upon comparing the refractive index of several commonly used particles (Fig. S3†), it was determined that the TiO_2 nanoparticles exhibit the most favorable refractive index, aligning best with our experimental requirements. However, the reflectance of the TiO_2 nanoparticles in the wavelength range of 200–400 nm is low due to the over-absorption of ultraviolet rays, which results in a decrease in reflectance. The reflectance of the GMs particles in the near-infrared spectrum is high, thereby enhancing the reflective performance of the SM film in that range. Reflectance tests conducted on REPs particles demonstrate their ability to improve the reflection in the 0.5–2.5 μm range. Therefore, we conclude that the three selected particles all meet the experimental requirements of high reflectivity.

In order to more effectively evaluate whether the addition of REPs enhances the cooling performance of the SM film, we conducted several sets of experiments by changing the doping ratio of REPs. The variation in the ratio of each component is presented in Table S1.† We also measured the reflectance of the sample films after incorporating different ratios of REPs. Fig. 2g illustrates the average reflectance of the films with varying ratios, and their detailed reflectance curves are displayed in Fig. S5a.† In order to make the reflection data more scientific, error analysis was performed for the reflection data with different proportions of REPs. The error analysis is shown in Fig. S5b.† By adjusting the ratio of REPs incorporated into the SM film, it can be concluded that the SM film with REPs of 12% exhibits the highest reflectivity. From Fig. 2g, it is evident that as the ratio of REPs increases, particles of varying sizes can be more effectively mixed, resulting in enhanced reflectivity of the film. However, when the ratio reaches a certain threshold, larger particles may obscure smaller ones, leading to a decrease in the scattering efficiency of the particles and, consequently, a reduction in the reflectance. Therefore, when the mass of REPs constitutes 12% of the total mass, the reflection performance of the SM film is optimized. We then conducted a comparative test to evaluate the reflectivity of the SM film against that of the WR film (Fig. 2h). The WR film does not incorporate REPs, while all other materials and experimental procedures remain consistent with those of the SM film. The test results indicate that the reflective properties of the SM film, which includes REPs, are superior to those of the WR film without REPs. This improvement can be attributed to the high inherent reflectivity of the REPs and the distinct particle size of the REPs compared to the other two particles, which enhances the scattering efficiency among the particles and increases the reflectivity of the SM film.

Fig. 3a illustrates that the primary components of the SM film and WR film are C, O and Si. The high-resolution C 1s spectra presented in Fig. 3b and c reveal the presence of chemical bonds, such as C–C, C=O, and C–Si. Fig. 3d and e display the FTIR spectra of the WR film and SM film, respectively. The absorption peaks at 787.41/787.54 cm^{-1} and 1257.41/1257.43 cm^{-1} correspond to the vibrational peaks of $-CH_3$ and the stretching peaks of C–Si in $Si–CH_3$.[39] The absorption peak at 1010.00/1009.82 cm^{-1} represents the antisymmetric stretching vibrational peak of Si–O–Si.[39,40] These features align with the structural characteristics of PDMS, whose structural formula and model diagram are depicted in Fig. S6.† Fig. 3f presents the spectral characteristics of REPs. In the visible range, the absorption decreases with increasing wavelength, as TiO_2 exhibits very high absorption properties for UV light.[31,32] The excitation wavelength of the REPs particles is 390 nm, while the emission wavelength is 470 nm. Hence, the doping of the REPs particles not only reduces the absorption rate of the SM film, but also competes with TiO_2 particles for absorbing UV. Additionally, it can effectively emit blue light, which mitigates the temperature rise caused by UV absorption in the radiation cooler.

As illustrated in Fig. 3g, we evaluated the photoluminescence properties of the REPs powder and SM film. The results indicate that the photoluminescence performance of the SM film is somewhat lower than that of the REPs powder. The optical cavity formed by the TiO_2 particles significantly influences the luminescence performance of the REPs.[17] As the fluorescence lifetime of the REPs decreases, a greater number of photons are converted by REPs, thereby enhancing the solar emissivity of the SM film. Fig. 3h presents a schematic diagram of the energy level transition of a rare earth particle. When irradiated by a laser, electrons in the valence band are excited and jump to the conduction band. During this process, some electrons directly undergo the characteristic leap $4f^7 \rightarrow 4f^6 5d^1$ of the Eu^{2+} ion and return to the ground state, resulting in photoluminescence.[41,42] According to Kirchhoff's law, the emissivity of a polymer film is determined by its absorptivity, the chemical bonds it contains, and the type of particles incorporated within it.[13] Due to the large size distribution of inorganic particles dispersed throughout the polymer matrix, the emissivity spectra exhibit broadband characteristics. Consequently, the emissivity of both the SM film and WR film exceed 0.9 at 3–20 μm, with the emissivity of the SM film reaching 0.95 at 8–13 μm, as shown in Fig. 3i and Table S2.†

To evaluate the cooling effect of the composite film, a temperature measuring device was constructed, with its schematic and physical drawings presented in Fig. 4a and S7.† The xenon lamp was set to a power output of 1100 W m^{-2} to simulate the sunlight conditions. The composite film was

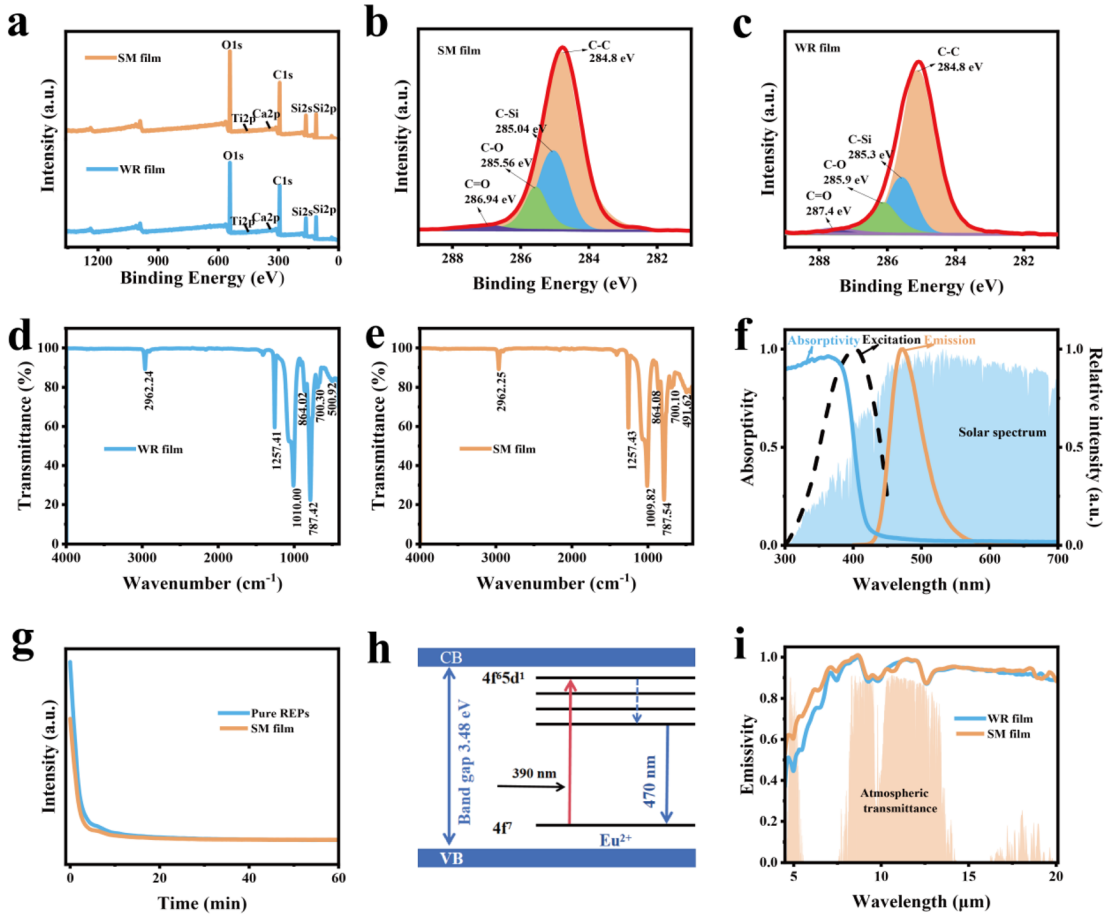

Fig. 3 Characterization and performance testing of the SM film and WR film. (a) Full spectrum analysis of the SM film and WR film using XPS. (b) High-resolution spectra of the C 1s region of the SM film. (c) High-resolution spectra of the C 1s region of the WR film. (d and e) FTIR spectra of the SM film and WR film. (f) Excitation, emission and absorption spectra of REPs particles. (g) Fluorescence lifetime mapping of REPs powder and SM film. (h) Schematic of the energy level transitions in REPs. (i) Emissivity of the SM film and WR film.

placed inside the cooling unit cavity, and covered with a polyethylene film avoid the influence of the external environment on the test. A K-type thermocouple was employed to record the temperature within the cavity beneath the composite film and the cavity beneath the PE film. The experimental results are illustrated in Fig. 4b. Fig. 4c depicts the temperature difference between the two sample membranes and the cooling unit cavity. The data indicate that, under xenon lamp irradiation, the cooling effect of the SM film with added REPs is superior to that of the WR film. When the xenon lamp is turned off, the SM films exhibit better insulation properties, resulting in a slower temperature drop compared to the WR films. This suggests that the SM film effectively inhibits excessive cooling. We then assessed the temperature performance of the two composite films under xenon lamp irradiation (Fig. 4d). In this scenario, the composite film was placed on a foam board and directly irradiated with the xenon lamp. As the irradiation time increased, the temperature of the WR film rose more rapidly than that of the SM film. In order to more conveniently observe the temperature variation trend in the sample film, we plotted a graph of the temperature data changing over time (Fig. 4e). The experimental results not only demonstrate that the SM film possesses superior cooling capabilities, but also indicate that the incorporation of the REPs particles enhances the cooling effect.

To better evaluate the scientific validity of the SM film's all-weather cooling performance, we simulated the data from the cooling unit using COMSOL software. Fig. 5a presents the model of the cooling device created with COMSOL software. Fig. 5b displays the simulation result obtained after inputting the weather data from June 9 into the software. By looking at the cross-section of the cooling device, we can intuitively see that the internal temperature of the entire device is different. The highest temperature is in the cavity covered by the PE film, which is the part that receives direct sunlight. The second is the SM film that we prepared. Finally, the lowest temperature was found in the cavity covered by the SM film. Owing to the excellent reflectivity and emissivity of SM film, its cavity temperature is the lowest, and this result is consistent with the actual test results. This further proves that our experimental results are scientific. As illustrated in Fig. 5b, the SM film demonstrates a significant cooling effect during the daytime when the sunlight is abundant, achieving a cooling performance of 17 °C at 12:00 noon. The cooling effect diminishes at

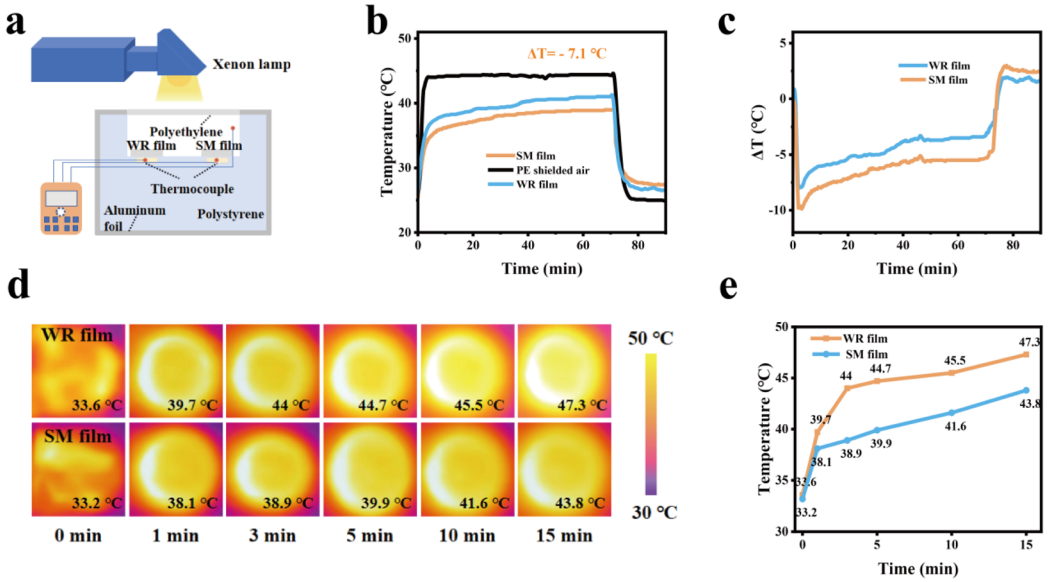

Fig. 4 Indoor cooling test. (a) Diagram of the temperature measuring device in the chamber. (b) Temperature data of the two composite films under 1100 W m^{-2} xenon lamp irradiation. (c) Temperature difference between the SM film and WR film and air under xenon lamp irradiation. (d) Infrared thermal images showing the surface temperature of the SM film and WR film under varying durations of xenon lamp irradiation. (e) Trend in temperature variation of the SM film and WR film over time under xenon lamp irradiation.

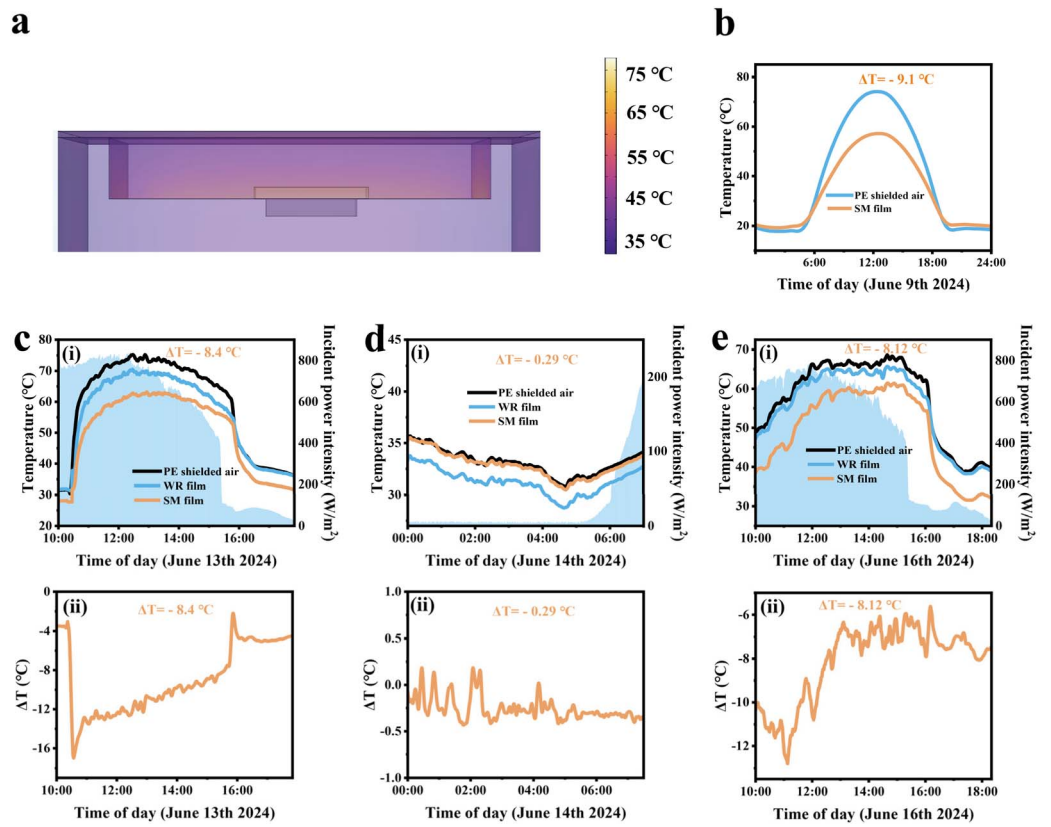

Fig. 5 Outdoor temperature simulated measurement experiments and actual outdoor temperature measurement experiments: (a) modeling of the outdoor temperature measurement device using COMSOL software. (b) Cooling simulation of the temperature measurement device using COMSOL software. (c) Plot of the outdoor temperature measurement data and cooling data on June 13th, 2024. (d) Plot of the outdoor temperature data and cooling data for June 14th, 2024. (e) Plot of the outdoor temperature measurement data and cooling data for June 16th, 2024.

night, and the device's ability to mitigate nighttime supercooling aligns with the objectives of our experimental design. Fig. 5c–e shows the results of our practical tests conducted during both daytime and nighttime with the cooling device. The schematic and physical representations of the outdoor cooling device are shown in Fig. S8.† By analyzing the data presented in the figures, it is evident that the SM film exhibits superior cooling performance. If the SM film is combined with the refrigeration system, the ambient temperature can be reduced very quickly. This will effectively alleviate the heavy use of energy for maintaining cooling, and play a role in saving energy.

As illustrated in Fig. 5c(i), during the daytime test conducted on June 13, when the average solar power was 705.4 W m^{-2}, the maximum temperature drop of the SM film reached 12 °C. The average temperature drop was 8.4 °C, and the temperature drop curve is presented in Fig. 5c(ii). Fig. 5d(i) demonstrates that, in the nighttime test on June 14, the maximum temperature drop was 0.45 °C. The average temperature drop at night was only 0.29 °C, and the corresponding temperature drop curve is depicted in Fig. 5d(ii). This suggests that the SM film can mitigate nighttime supercooling. As demonstrated in Fig. 5e(i), during the daytime test on June 16, the maximum cooling effect of the SM film reached 11 °C when the average solar power was 608 W m^{-2}. The average temperature difference was 8.12 °C, and the cooling curve is shown in Fig. 5e(ii). The actual outdoor test results of the cooling device are largely consistent with the simulation results, indicating that the SM film possesses effective radiative cooling performance during the day and inhibited supercooling at night. Additionally, we compared our fabricated radiative cooler with previously reported radiative coolers, as shown in Table S2.† Our radiative coolers demonstrate significantly high reflectivity, high emissivity, and most importantly, exceptional radiative cooling performance during real-world outdoor tests.

We then covered the top of the house model with the SM film to evaluate its radiative cooling performance (Fig. 6a). The temperature data were recorded using an infrared camera, and

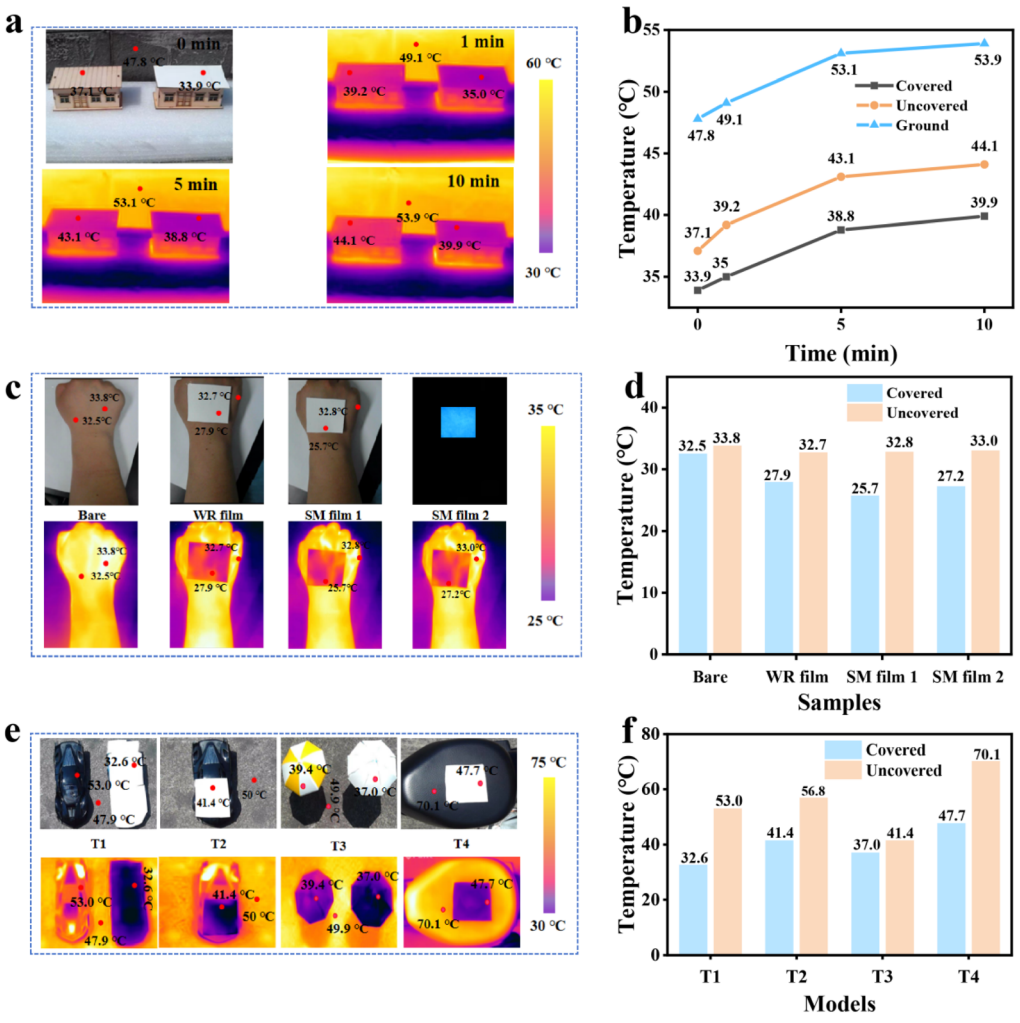

Fig. 6 Radiative cooling characteristics of the SM film and WR film measured using an IR camera. The models employed in this study are scaled-down versions. (a) Temperature data of the ground, bare roof, and roof covered with the SM film recorded using an infrared camera. (b) Data presented in (a) were plotted as a line graph. (c) Temperature data of the bare arm and arm covered with different films recorded by an infrared camera. (d) Plot of the data in (c) as a bar graph. (e) Temperature data for a car model, sunshade, and e-bike seat cushion recorded from their exposed surface and position covered with the SM film using an infrared camera. (f) Data from (e) plotted as a bar graph.

are presented in Fig. 6b. As illustrated in Fig. 6b, we began recording the temperature at 0 minutes and continued recording for a duration of 10 minutes. During this period, the temperature gradually increased, with the temperature difference for the house model covered by the SM film measuring 14.1 °C. Meanwhile, the average temperature difference for the house model without the film was 10.1 °C. In comparison, the house model covered with the SM film exhibited a more pronounced cooling effect, enhancing the cooling performance by 4 °C. If the SM film is applied to the roof of the building, it can effectively reduce the building's temperature, and protect it from direct sunlight, thereby extending its service life.

Fig. 6c illustrates the temperature data recorded by the infrared camera for the arm covered with different films for 3 minutes, and the infrared imaging temperature under dark conditions. The data for the four cases were compiled and are presented in Fig. 6d. As shown in Fig. 6d, the temperature of the arm covered with film is lower than that of the arm without a film. The cooling effect of the arm covered with the SM film is more pronounced than that of the arm covered with the WR film, with a maximum temperature difference of 7.1 °C. Under dark conditions, the temperature difference for the arms covered with the SM film is smaller than that observed under bright conditions, indicating that the SM film possesses the capacity to inhibit supercooling under dark conditions. Furthermore, the incorporation of REPs particles during the production process of the SM film enables it to exhibit a fluorescence effect under dark conditions, which can serve as a warning signal for individuals in a dark environment.

As shown in Fig. 6e, we applied the SM film to the surfaces of various objects to evaluate its cooling effect. The data were subsequently organized and are presented in Fig. 6f. The figure demonstrates that when the car model is covered with the SM film, the temperature difference compared to the uncovered model reaches 20.4 °C. In the car model that is partially covered with the SM film, the temperature difference between the covered and uncovered areas is 15.4 °C. If the SM film is utilized to create sun protective clothing and sunshade, it lowers the temperature inside the car and also mitigates the impact of direct sunlight on the car. We tested the radiative cooling effect by applying the SM film to beach umbrellas and e-bike seats. As illustrated in the figure on the right, it can be seen that the temperature of the sunshade can be effectively reduced by when covered with the SM film, compared to a reduction of 8.5 °C for a beach sunshade without the film. This demonstrates that the application of the SM film significantly enhances the cooling efficiency of sunshade, creating a more comfortable environment for people. Additionally, when applied to an electric bicycle seat, the temperature can be reduced by an impressive 22.4 °C. If the SM film is commercially utilized, it has the potential to provide a comfortable living space for individuals during the hot summer day. Our cooling tests, which involved covering the surfaces of various objects with the SM film, demonstrate that our samples not only exhibit excellent cooling performance, but also possess promising market application prospects.

In addition to the excellent optical properties of the SM film, we also evaluated its flexibility, hydrophobicity and self-cleaning ability. As illustrated in Fig. S9,† we assessed the flexibility and stress change effect of the sample mold by twisting and rolling it. Fig. S9a and b† demonstrate that the sample film we prepared exhibits remarkable flexibility. Tensile instruments were also employed to measure the impact of stress changes on the sample film. The maximum strain of the SM film reaches 68%, with a pulling force of 13.1 N (Fig. S9c†). In comparison, the maximum strain of the WR film reaches 63.6%, with a pulling force of 12.7 N (Fig. S9d†). As illustrated in Fig. S10a,† four different beverages (cola, Fanta, milk, and water) were applied to the sample mold. Observations indicated that the liquid maintained a spherical shape, suggesting that the sample mold exhibits significant hydrophobic properties. Additionally, we assessed the excellent hydrophobicity of the SM film by depositing several water droplets with varying volumes onto the sample mold. The measured static water contact angle was approximately 120°. Fig. S11† demonstrates the self-cleaning performance of the SM film, as fine sand was sprinkled onto the surface to simulate the erosion of the external dust environment. Upon rinsing with water, it was evident that the fine sand can be easily removed from the SM film. If the SM film is utilized on the building wall, it could not only contribute to a reduction in indoor temperature but also effectively mitigate the impact of environmental erosion on the building.

3 Conclusions

In summary, we have integrated particle scattering, sun-induced fluorescence particle emission and broadband radiative cooling to develop an all-weather broadband radiative cooling composite film. Particles with varying sizes enhance the scattering efficiency of the film, while the incorporation of fluorescent particles facilitates the outward emission of energy in the form of visible light. The broadband radiative mechanism employs the sky as a temperature regulator, thereby minimizing temperature differentials. This integration approach not only improves the reflectivity and emissivity of the cooling device, but also effectively reduces the temperature. Our results show that the SM film can provide radiant cooling during the day, while effectively suppressing excessive cooling at night. In addition, by testing the flexibility, hydrophobicity, self-cleaning performance and night fluorescence warning effect of the film, our designed radiation cooling composite film has a wide range of application potential in daily life. This radiation-cooled composite film is not only suitable for the cooling of buildings, but also for other material surfaces that require radiation cooling. The PDRC system design concept presented here has significant advantages, including ease of manufacturing, cost effectiveness, high performance and versatility, positioning it as a promising solution for advancing green development.

4 Experiment

4.1 Materials and method

Materials: the PDMS polymer (SYLGARDTM 184) and curing agent were supplied by Dow Corning provided. REPs

($Sr_2MgSi_2O_7:Eu^{2+},Dy^{3+}$) were provided by Foshan Gaoliang Phosphor Co., Ltd. TiO_2 nanoparticles (100–600 nm) were purchased from McLean Biotechnology, Shanghai, China. GMs were obtained from 3M Co., Ltd. Ethyl acetate (EAC) was supplied by Aladdin Biotechnology, Shanghai, China. Method: the composite film samples were composed of PDMS (16 wt%), REPs (3.4 wt%), TiO_2 (5.9 wt%), GMs (2.7 wt%) and EAC (72 wt%), and were designated as the SM film. The mass ratios of PDMS, REPs, TiO_2, and GMs in each sample are clearly presented in Table S1.† To demonstrate the effectiveness of REPs ($Sr_2MgSi_2O_7:Eu^{2+},Dy^{3+}$) for radiative cooling, we fabricated WR films without REPs to compare their optical performances, and the other components of the WR films were identical to those in the SM film. The experimental preparation steps for the sample mold and the instruments used are illustrated in Fig. S1.† First, we added PDMS and curing agent to a beaker containing EAC solution at a mass ratio of 10 : 1. The solution was then stirred at 500 rpm for two hours at 28 °C, during which the TiO_2 nanoparticles and REPs particles were incorporated. Next, the stirring speed was reduced and the GMs powder was added to the solution. The mixture was stirred for 10 minutes and then sonicated for 10 minutes, with this process being repeated twice. The speed was lowered to prevent the GMs from breaking up during mixing, while sonication was employed ensure even distribution of the filler particles. To eliminate air bubbles during the drying of the film, we poured the solution into a Petri dish and placed it into a vacuum freeze dryer for 5 minutes to evacuate the air. Finally, the sample film was dried in a blast oven at 50 °C for 3 hours. The preparation method for the control film is basically the same as that of the SM film. A detailed schematic diagram of the preparation processes for the SM and WR films is presented in Fig. S1.†

4.2 Characterization

A UV-Vis-NIR spectrophotometer (Shimadzu UV3600) was used to measure the reflectance of the sample films within the 0.3–2.5 μm band. The microstructure of the samples and the distribution of particles inside the films were observed by a field emission scanning electron microscope (SEM, Carl Zeiss 300), and the distribution of elements was detected using an energy dispersive spectroscopy (EDS) module. Fourier transform infrared spectroscopy (FTIR, Thermo Nicolet IS5) and X-ray photoelectron spectroscopy (XPS, Thermo Kalpha) were employed to determine the chemical bonding composition of all sample films. The purity of the sample powders and the structural phase composition were investigated using an X-ray diffractometer (XRD, Shimadzu XRD-6100). The hydrophobicity of the sample films was characterized using an optical contact angle meter (JY-82B Kruss DSA). The excitation and emission spectra of the rare earth phosphors were measured by a fluorescence spectrometer (FL3-211).

4.3 Cooling performance tests

The radiation-cooled model was constructed using the SM film, WR film, foam box, aluminum foil, and polyethylene film (PE). Additionally, some SM films were covered on the arms, beach umbrella models, and car models to evaluate the cooling effect. The surface temperature variation of the sample mold was recorded by an infrared camera (FLIR ONE PRO). For the indoor cooling experiments, a xenon lamp was used to simulate the sunlight irradiation and a thermocouple (TA612C) was used to record the temperature change data of the cooling device. In the outdoor cooling experiments, the temperature and light power were recorded using a K-type thermocouple and an optical power meter (TES1333R).

Data availability

The authors will supply the relevant data on reasonable requests.

Author contributions

Gongxun Bai, Qingong Hu, and Peng Xue conceived the concept and flow of this study. Qinglong Hu and Pengjie Zhong drew the schematic diagrams. Qinglong Hu and Ruiming Tan prepared the experimental samples. Qinglong Hu and Yinyan Li simulated the experimental results. Qinglong Hu, Keyu Han, Peng Xue, and Gongxun Bai wrote the manuscript. All authors discussed the experimental structure and commented on the manuscript. All authors have accepted responsibility for the full content of this manuscript and approved its submission.

Conflicts of interest

The authors declare no conflicts of interest.

Acknowledgements

This work was financed by the National Key Research and Development Program of China (2021YFB3502100), and the Natural Science Foundation of Zhejiang Province (LR24F050002).

References

1 R. Wu, C. Sui, T. Chen, Z. Zhou, Q. Li, G. Yan, Y. Han, J. Liang, P. Hung, E. Luo, D. V. Talapin and P. Hsu, *Science*, 2024, **6701**, 1203–1212.
2 X. Zhao, T. Li, H. Xie, H. Liu, L. Wang, Y. Qu, S. Li, S. Liu, A. H. Brozena, Z. Yu, J. Srebric and L. Hu, *Science*, 2023, **6671**, 684–691.
3 W. Tang, Y. Zhan, J. Yang, X. Meng, X. Zhu, Y. Li, T. Lin, L. jiang, Z. Zhao and S. Wang, *Adv. Mater.*, 2024, **36**, 2310923.
4 J. Zhou, T. G. Chen, Y. Tsurimaki, S. Fan, M. Cutkosky and Y. Cui, *Joule*, 2023, **7**, 2830–2844.
5 M. Huang, M. Yang, X. Guo, C. Xue, H. Wang, C. Ma, Z. Bai, X. Zhou, Z. Wang, B. Liu, Y. Wu, C. Qiu, C. Hou and G. Tao, *Prog. Mater. Sci.*, 2023, **137**, 101144.
6 C. Wang, H. Chen and F. wang, *Prog. Mater. Sci.*, 2024, **144**, 101276.
7 J. Yang, X. Zhang, X. Zahng, L. Wang, Q. Li and W. Feng, *Adv. Mater.*, 2021, **14**, 2004754.

8 X. Yin, R. Yang, G. Tan and S. Fan, *Science*, 2020, **370**, 786–791.
9 B. Li, C. Valenzuela, Y. Liu, X. Zhang, Y. Yang, Y. Chen, L. Wang and W. Feng, *Adv. Funct. Mater.*, 2024, **34**, 2402124.
10 J. Woods, N. James, E. Kozubal, E. Bonnema, K. Brief, L. Voeller and J. Rivest, *Joule*, 2022, **6**, 726–741.
11 Y. Fu, L. Chen, Y. Guo, Y. Shi, Y. Liu, Y. Zeng, Y. Lin and D. Luo, *Adv. Sci.*, 2024, **11**, 2404900.
12 A. Aili, D. Zhao, G. Tan, X. Yin and R. Yang, *Appl. Energy*, 2021, **302**, 117515.
13 R. Tan, W. Hu, X. Yao, N. Lin, P. Xue, S. Xu and G. Bai, *J. Mater. Chem. C*, 2024, **12**, 2629–2638.
14 S. Fan and W. Li, *Nat. Photonics*, 2022, **16**, 182–190.
15 T. Wang, Y. Wu, L. Shi, X. Hu, M. Chen and L. Wu, *Nat. Commun.*, 2021, **12**, 365.
16 X. Yin, R. Yang, G. Tan and S. Fan, *Science*, 2020, **6518**, 786–891.
17 X. Xue, M. Qiu, Y. Li, Q. Zhang, S. Li, Z. Yang, C. Feng, W. Zhang, J. Dai, D. Lei, W. Jin, L. Xu, T. Zhang, J. Qin, H. Wang and S. Fan, *Adv. Mater.*, 2020, **32**, 1906751.
18 K. Tang, K. Dong, J. Li, M. Gordon, F. Reichertz, H. Kim, Y. Rho, Q. Wang, C. Lin, C. Grigoropoulos, A. Javey, J. Urban, J. Yao, R. Levinson and J. Wu, *Science*, 2021, **6574**, 1504–1509.
19 D. Wu, C. Liu, Z. Xu, Y. Liu, Z. Yu, L. Yu, L. Chen, R. Li, R. Ma and H. Ye, *Mater. Des.*, 2018, **139**, 104–111.
20 H. Zhong, P. Zhang, Y. Li, X. Yang, Y. Zhao and Z. Wang, *ACS Appl. Mater. Interfaces*, 2020, **12**, 51409–51417.
21 D. Chae, S. Son, Y. Liu, H. Lim and H. Lee, *Adv. Sci.*, 2020, **7**, 2001577.
22 A. Leroy, B. Bhatia, C. Kelsall, A. Castillejo-Cuberos, H. Di-Capua, L. Zhao, L. Zhang, A. Guzman and E. Wang, *Sci. Adv.*, 2019, **5**, eaat9480.
23 Z. Lu, E. Strobach, N. Chen, N. Ferrialis and J. Grossman, *Joule*, 2020, **4**, 2693.
24 X. Li, J. Peoples, P. Yao and X. Ruan, *ACS Appl. Mater. Interfaces*, 2021, **13**, 21733–21739.
25 M. Aladailah, O. Tashlykov, T. Volozheninov, D. Kaskov, K. Iuzbashieva, R. Al-Abed, A. Acikgoz, N. Yorulmaz, M. Yas-ar, W. Al-Tamimi and M. Alshipli, *Opt. Mater.*, 2022, **134**, 113197.
26 R. Yalçın, E. Blandre, K. Joulain and J. Drévillon, *ACS Photonics*, 2020, **7**, 1312–1322.
27 X. Wu, J. Li, F. Xie, X. Wu, S. Zhao, Q. Jiang, S. Zhang, B. Wang, Y. Li, D. Gao, R. Li, F. Wang, Y. Huang, Y. Zhao, Y. Zhang, W. Li, J. Zhu and R. Zhang, *Nat. Commun.*, 2024, **15**, 815.
28 J. Wang, J. Sun, T. Guo, H. Zhang, M. Xie, J. Yang, X. Jiang, Z. Chu, D. Liu and S. Bai, *Adv. Mater. Technol.*, 2022, **7**, 2100528.
29 Y. Peng, L. Fan, W. Jin, Y. Ye, Z. Huang, S. Zhai, X. Luo, Y. Ma, J. Tang, J. Zhou, L. Greenburg, A. Majumdar, S. Fan and Y. Cui, *Nat. Sustainable*, 2021, **5**, 339–347.
30 T. Wang, Y. Zhang, M. Chen, M. Gu and L. Wu, *Cell Rep. Phys. Sci.*, 2022, **3**, 100782.
31 J. Li, Y. Fu, J. Zhou, K. Yao, X. Ma, S. Gao, Z. Wang, J. Dai, D. Lei and X. Yu, *Sci. Adv.*, 2023, **9**, eadg1837.
32 X. Ma, Y. Fu, A. Portniagin, N. Yang, D. Liu, A. Rogach, J. Dai and D. Lei, *J. Mater. Chem. A*, 2022, **10**, 19635–19640.
33 D. Keith, G. Holmes, D. Angelo and K. Heidel, *Joule*, 2018, **8**, 1573–1594.
34 D. Zhao, A. Aili, Y. Zhai, S. Xu, G. Tan, X. Yin and R. Yang, *Appl. Phys. Rev.*, 2019, **6**, 021306.
35 P. Poredoš, H. Shan, C. Wang, Z. Chen, Z. Shao, F. Deng, H. Liu, J. Yu and R. Wang, *Energy Environ. Sci.*, 2024, **17**, 2336–2355.
36 A. Raman, M. Anoma, L. Zhu, E. Rephaeli and S. Fan, *Nature*, 2014, **515**, 540–544.
37 H. Tang, C. Guo, F. Fan, H. Pan, Q. Xua and D. Zhao, *Energy Environ. Sci.*, 2024, **17**, 4498–4507.
38 D. Chae, H. Lim, S. So, S. Son, S. Ju, W. Kim, J. Rho and H. Lee, *ACS Appl. Mater. Interfaces*, 2021, **13**, 21119–21126.
39 Y. Tian, H. Shao, X. Liu, F. Chen, Y. Li, C. Tang and Y. Zheng, *ACS Appl. Mater. Interfaces*, 2021, **13**, 22521–22530.
40 Z. Sun, J. Wen, W. Wang, H. Fan, Y. Chen, J. Yan and J. Xiang, *Prog. Org. Coat.*, 2020, **146**, 105744.
41 J. Luo, B. Ren, X. Zhang, M. Zhu, T. Liang, Z. Huang, Y. Zheng, X. Li, J. Li, Z. Zheng, B. Chen, Y. Fu, D. Tu, Y. Wang, Y. Jia and D. Peng, *Adv. Sci.*, 2024, **11**, 2305066.
42 J. Ma, F. Zeng, X. Lin, Y. Wang, Y. Ma, X. Jia, J. Zhang, B. Liu, Y. Wang and H. Zhao, *Science*, 2024, **6704**, 68–74.

